NESS1: A Worldwide Collection of Strong-Motion Data to Investigate Near-Source Effects

by Francesca Pacor, Chiara Felicetta, Giovanni Lanzano, Sara Sgobba, Rodolfo Puglia, Maria D'Amico, Emiliano Russo, Georgios Baltzopoulos, and Iunio Iervolino

ABSTRACT

The availability of high-quality waveforms recorded in epicentral areas of moderate-to-strong earthquakes is a key factor for investigating ground-motion characteristics close to the seismic source. In this study, near-source strong-motion waveforms (named NESS1) were collected from worldwide public archives with the aim of building a flat file of high-quality metadata and intensity measures (IMs) of engineering interest. Particular attention was paid to the retrieval of reliable information about event sources, such as geometries and rupture mechanisms that are necessary to model near-source effects for engineering seismology and earthquake engineering applications. The accelerometric records are manually and uniformly processed, and the associated information is fully traceable. NESS1 consists of about 800 three-component waveforms relative to 700 accelerometric stations, caused by 74 events with moment magnitude larger than 5.5 and hypocentral depth shallower than 40 km, with Joyner–Boore distance up to 140 km. Ground-motion data were selected to have a maximum source-to-site distance within one fault length, defined through seismological scaling relations. About 40 records exhibit peak acceleration or peak velocity exceeding 1*g* or 120 cm/s, and they represent some of the largest ground motion ever recorded. Evidence of near-source effects was recognized in the NESS1 dataset, such as velocity pulses, large vertical ground motions, directional and hanging-wall amplifications and fling step. In particular, around 30% of the records was found to exhibit pulse-like characteristics that are possibly due to forward rupture directivity.

Electronic Supplement: Table listing the main features of the selected events, including the references of fault geometry parameters and Figures showing further metadata and intensity measures distributions of the NESS1 flat file.

INTRODUCTION

The availability of waveforms from moderate-to-strong events recorded in epicentral areas is a relevant need for earthquake engineering and engineering seismology purposes. This is demonstrated by the increasing number of studies in the last decades that were focused on the characterization of ground-motion effects in the near-source region, particularly after the 1999 M_w 7.6 İzmit (Turkey) event (e.g., Campbell and Bozorgnia, 2003; Mavroeidis and Papageorgiou, 2003; Somerville, 2003; Bray and Rodriguez-Marek, 2004; Chioccarelli and Iervolino, 2010). These studies pointed out that ground motion recorded close to the seismic source may show features that are responsible for peculiar seismic demand imposed on structures situated in epicentral area (e.g., Champion and Liel, 2012; Iervolino *et al.*, 2012).

Typical and well-known effects observed in the near-source regions include the vertical component exhibiting much larger amplitude than the corresponding horizontal component, pulse-like ground motion due to forward directivity, a fling-step effect due to permanent tectonic displacement, and hanging-wall (HW) or footwall (FW) systematic difference. Polarization of motion, or directionality, is also observed in strong-motion data recorded close to the source (Shahi and Baker, 2014).

Several attempts have been carried out to model HW (e.g., Donahue and Abrahamson, 2014) and directivity effects (e.g., Spudich *et al.*, 2014), as well as the amplitude of fling step (e.g., Faccioli *et al.*, 2004; Kamai *et al.*, 2014; Burks and Baker, 2016). On the other hand, despite the relevant impact and engineering significance of the ground-motion characteristics in near-source conditions, few attempts have been made to account for them in seismic code provisions (Tothong *et al.*, 2007; Grimaz and Malisan, 2014; Baltzopoulos *et al.*, 2015).

Ground-motion prediction equations (GMPEs) typically seek to account for such effects as a function of a few explanatory variables (e.g., magnitude, source-to-site distance, azimuth between the fault strike and the observer). However, existing models produce results that may significantly differ from one to another, mainly due to the paucity of near-source records and the lack of adequate knowledge and/or a high level of

doi: 10.1785/0220180149

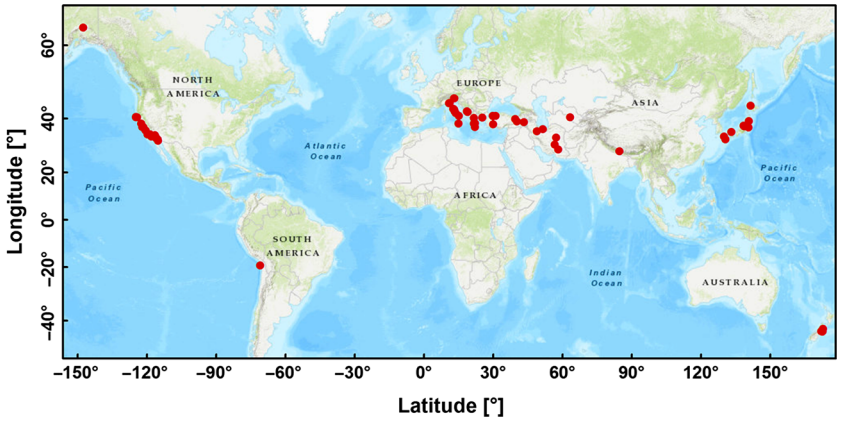

▲ **Figure 1.** Map of the epicentral distribution of the 74 worldwide earthquakes included in near-source strong-motion waveforms (NESS1). The color version of this figure is available only in the electronic edition.

uncertainty in the characterization of the fault geometry, which is essential information to model the mentioned effects.

Another issue concerns the modeling of the distance scaling in near-source regions that is only captured by the classical GMPEs up to some extent, because typical distance metrics have, in general, limited explanatory power with respect to the effects of the rupture propagation and slip distribution on an extended fault (Thompson and Baltay, 2018).

To contribute to addressing these issues, we compiled a dataset of near-source strong-motion records and metadata suitable for seismic response analysis and ground-motion studies in proximity to the seismic source. This near-source ground-motion dataset (hereinafter referred as NESS1), is a collection of 800 worldwide records, selected from various repositories of accelerometric data, according to specific criteria in terms of moment magnitude ($M_w \geq 5.5$) and distance. In particular, ground-motion data were selected to have a maximum source-to-site distance proportional to the fault length, defined through seismological scaling relations.

A fundamental step in the compilation of the NESS1 was to retrieve adequate information about event-source geometries and rupture mechanisms that allowed the calculation of different metrics to define the source-to-site configuration. Moreover, only raw waveforms available on public repositories were selected and manually processed to construct a homogeneous dataset of ground-motion intensity measures (IMs). The suitability of NESS1 to represent the ground motion in the near source is shown by evidence of velocity pulses, large vertical components, polarized ground motions, and HW effects that were identified via a preliminary analysis.

DATASET

To construct a dataset of accelerometric waveforms potentially affected by near-source effects, worldwide active-crustal earthquakes (Fig. 1) were initially selected according to the following criteria: (1) moment magnitude (M_w) greater than or equal to 5.5, (2) hypocentral depth less than 40 km, (3) availability of geometrical information on the finite-fault model, and (4) availability of strong-motion records in epicentral areas and in free-field conditions.

For the selected events, only raw waveforms were collected and then uniformly processed to compute the IMs. The near-source strong-motion dataset was arranged as a table (named NESS1 flat file) that contains verified and reliable metadata and IMs of the manually processed waveforms. The fields of the flat file are consistent with the Engineering Strong-Motion (ESM) flat file (Lanzano *et al.*, 2018) and can be grouped into six main blocks of metadata: (1) event-related, (2) source-related, (3) station-related, (4) metrics of source-to-site distances, (5) waveform-related, and (6) ground-motion IMs. The NESS1 webpage provides access to the flat file and to related documents (field dictionaries and user manual).

Earthquakes

To build the dataset, we identified 74 worldwide events with $M_w \geq 5.5$ (see Ⓔ Table S1, available in the electronic supplement to this article). For 60 earthquakes, fault geometries were retrieved from published studies or from regional and worldwide databases (see Data and Resources). The saved information includes: strike, dip, and rake angles, the depth of the top of rupture plane, the fault length and width, and the coordinates of the reference point that are needed to compute different source-to-site distances. In case of events with multisegment rupture (e.g., 2002 M_w 7.9 Denali, Alaska; 2011 M_w 6.6 Fukushima Homadoru, Japan; 2016 M_w 7.0 Kumamoto-shi, Japan), the parameters of the dominant fault segment were considered.

Hypocentral coordinates and moment magnitude were recovered after consulting multiple catalogs (see Data and Resources) and specific event studies. For the oldest events, the instrumental hypocenter provided by catalogs may fall beyond the edges of the proposed fault geometry. For this reason, in addition to the coordinates of the instrumental hypocenter, the coordinates of the starting point of the rupture on the fault plane (namely the nucleation point) were also included.

For the other 14 events (Ⓔ Table S1) having high-quality strong-motion records in the epicentral area, it was not possible to obtain complete finite-source models. In these cases, the strategy of simulating the fault geometry (virtual fault, in Ⓔ Table S1) or some missing parameters were adopted, modifying the procedure by Kaklamanos *et al.* (2011). The input parameters for virtual-fault calculation are the moment magnitude M_w, the strike and dip of the fault-plane solutions of moment tensor, and the hypocentral depth. The basic steps are: (1) calculating the fault length L and width W through empirical correlations in the function of M_w (Wells and Coppersmith, 1994); (2) setting the coordinates of the nucleation points equal to the hypocentral ones; (3) computing the

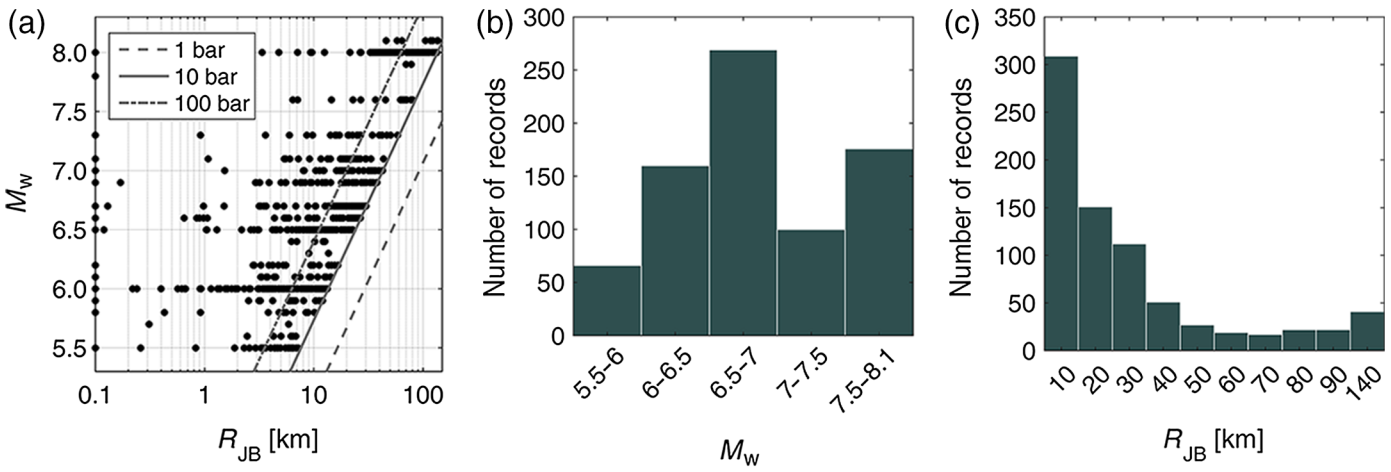

▲ **Figure 2.** Data distribution of NESS1: (a) magnitude M_w versus Joyner–Boore distance R_{JB}. Lines represent the scaling of the near-source distance in the function of magnitude and stress drop, according to equation (1) and $k = 1$, (b) number of waveforms as a function of M_w, and (c) Joyner–Boore distance R_{JB}. The color version of this figure is available only in the electronic edition.

points coordinates of the fault surface projection, assuming the location of the nucleation point at 1/2 L and 2/3 W from the top edge of the fault; (4) and, finally, calculating the depth of the top of the fault and the fault trace, obtained from the extension of the fault plane up to surface.

The focal mechanism of the events was assigned in accordance to the rake angle of the literature source models or to the solution of the moment tensor provided by the regional and international catalogs, using the convention of Aki and Richards (1980), with the modification of Boore *et al.* (1997) for strike-slip events.

Strong-Motion Waveforms

To select a number of accelerometric data possibly showing near-source features, it was assumed that such effects occurred in a limited area around the source, that is, within a few times the fault length. By applying the classical seismological scaling relations (Lay and Wallace, 1995) among seismic moment, slip on the fault and static stress drop $\Delta\sigma$, and the relationship between seismic moment and moment magnitude M_w (Hanks and Kanamori, 1979), a threshold distance R_{ns} (near-source distance), proportional to the fault length, was defined as follows:

$$\log(R_{ns}) = \log(k) + \frac{1}{2}M_w - \frac{1}{3}\log(\Delta\sigma) + 3.134, \qquad (1)$$

in which R_{ns} is given in m and $\Delta\sigma$ is in Pa, k is a parameter used to quantify how many fault lengths the sites should be away from the fault, to be considered within the region of interest.

The NESS1 dataset features strong-motion data recorded by stations located in the near-source region, according to the conventional criterion of equation (1) with $k = 1$ that is within one fault length and static stress drop that is equal to 10 bars, the latter representing the average value for moderate and strong events (Allmann and Shearer, 2009). As the distance metric, the Joyner–Boore distance, such as $R_{JB} \le R_{ns}$, was considered. As an example, the near-source regions for magnitude 6.5 and magnitude 7.0 earthquakes extend up to 25 and 40 km, respectively, from the surface projection of the faults (Fig. 2).

The choice of one fault length, although arbitrary, is roughly consistent with evidence of near-source effects in other studies (e.g., Chioccarelli and Iervolino, 2010).

Applying the above-mentioned criteria to the 74 events, the dataset resulted in 770 waveforms recorded by 666 different accelerometric stations. The majority of the events (Fig. 1) are located in the United States (18 events) and Italy (18 events). Japan and Turkey contribute with nine and seven events, respectively. The remaining earthquakes are distributed among Iran (five events), Greece (five events), New Zealand (five events), Montenegro (two events), Mexico (two events), Nepal (one event), Uzbekistan (one event), and Chile (one event).

The oldest earthquake included is the well-known 1933 M_w 6.4 Long Beach event that contributes with only a single record to the dataset, whereas the most recent ones are the 2016 M_w 8.0 Kaikōura (New Zealand), the 2016 M_w 7.0 Kumamoto-shi (Japan), and the 2016 M_w 6.5 Norcia (Italy) earthquakes that are also the most sampled events, with more than 30 waveforms. The event with the largest magnitude corresponds to the 2014 M_w 8.1 Chilean earthquake.

Source-to-Site Distance

Close to the seismic source, the point source-to-site distance measures (epicentral and hypocentral distance) that describe the scaling of ground-motion intensity are usually replaced by metrics based on the geometry of the finite-fault rupture plane. The distance measurements obtained using different metrics can differ significantly, especially in proximity to the source (see Ⓔ Fig. S1). Therefore, for the NESS1 records, six source-to-site distance measurements introduced into the Next Generation Attenuation-West2 (NGA-West2) Project

Table 1
Notation and Description of the Distance Measures

Distance Measures	Description
R_{EPI}	Epicentral distance: distance from epicenter
R_{HYP}	Hypocentral distance: distance from hypocenter
R_{JB}	Joyner–Boore distance: distance computed from the surface projection of the fault
R_{RUP}	Rupture distance: shorter distance to the rupture plane
R_X	Horizontal distance measured perpendicular to the fault strike from the top edge of rupture plane
R_{Y0}	Horizontal distance off the surface projection of rupture plane measured parallel to the fault strike.
R_{NP}	Nucleation point distance: distance from nucleation point
R_{LINE}	Shorter distance from the top edge of rupture plane computed as $\sqrt{R_X^2 + R_{Y0}^2}$

database (Ancheta *et al.*, 2014) were computed: epicentral distance R_{EPI}, hypocentral distance R_{HYP}, Joyner–Boore distance R_{JB}, rupture distance R_{RUP}, horizontal distance measured perpendicular to the fault strike R_X, and horizontal distance off the surface projection of the rupture plane measured parallel to the fault strike R_{Y0}. In addition, the distance from the nucleation point (R_{NP}) and from the top edge of rupture plane (R_{LINE}) were also calculated (Table 1).

Metadata Distribution

The dataset covers distances of up to 140 km when measured in R_{JB} terms, with the bulk of the records in the magnitude range 6.0–7.5 and with distances between 0 and 30 km (Fig. 2). About half of the waveforms (300) were recorded at $R_{JB} < 10$ km, and 45 waveforms were recorded over the surface projection of the fault ($R_{JB} = 0$).

Normal, strike-slip, and thrust focal mechanisms are included in the dataset, with a dominance of strike-slip events mainly located in the United States, New Zealand, and Turkey. Normal mechanisms are typical of Italy and Japan, whereas almost half of the thrust events are located in the United States (see Ⓔ Fig. S2).

Average shear-wave velocity in the uppermost 30 m (V_{S30}) was assigned to all recording stations (Ⓔ Fig. S2). When a direct measurement of the *S*-wave velocity profile was not available, V_{S30} was estimated by empirical correlation with the topographic slope, as proposed by Wald and Allen (2007) using a 90 m digital elevation map (DEM, digital elevation map provided by the Shuttle Radar Topography Mission). The majority of strong-motion data was recorded on soil ($V_{S30} < 600$ m/s) and only 8% on rock sites ($V_{S30} > 800$ m/s). In the flat file, the soil categories relative to the National Earthquake Hazards Reduction Program (NEHRP) (BSSC, 2003) and the EC8 (Comite Européen de Normalisation [CEN], 2004) classifications are included, associated using measured V_{S30} values, where available (if not, estimated V_{S30} is used for the former and surface geological information for the latter).

Waveform Processing

The accelerometric data were downloaded from different worldwide databases (see Data and Resources) in raw version and manually corrected by using the processing tool (Puglia *et al.*, 2018) developed within the ESM database (Luzi *et al.*, 2016). This tool implements the procedure described in Paolucci *et al.* (2011) and detailed in Pacor, Paolucci, Ameri, *et al.* (2011) that entails the application of a second-order acausal time-domain Butterworth filter to the zero-padded acceleration time series and zero-pad removal to make acceleration and displacement consistent after double integration.

Most of the digital waveforms, that constitute about 70% of the dataset, are filtered with high-pass frequencies of ≤ 0.1 Hz, whereas analog data are, on average, filtered at frequencies around 0.2 Hz, due to their lower quality. In both cases, the value of the low-frequency cutoff tends to decrease with increasing magnitude.

For each waveform component (horizontals as recorded and vertical), peak (peak ground acceleration [PGA], peak ground velocity [PGV], and peak ground displacement [PGD]) and integral IMs (significant duration, Housner, and Arias intensities) were computed from the processed waveforms. Furthermore, the 5% damped acceleration response spectra (SA) values are calculated for 36 ordinates in the natural vibration period range 0.01–10 s.

Several other IMs of horizontal ground motion, such as the geometrical mean, the fault-normal (FN) and fault-parallel (FP) components (i.e., normal and parallel to the fault strike), rotated with respect to the fault strike, the maximum (D100), the minimum (D00), and the median (D50) values of the ground-motion parameters, were obtained rotating the time series over all orientations (Boore, 2010).

Peak Ground-Motion Distributions

The dataset is characterized by relatively large ground motions: about 50% of the records have horizontal PGAs and PGVs larger than 0.2*g* and 23 cm/s, whereas 2% have PGAs and PGVs exceeding 1*g* and 100 cm/s, respectively (Fig. 3). The values of the vertical distributions are smaller than the horizontal ones but tend to increase in the upper percentiles, mainly for high-frequency ground-motion parameters.

Following Anderson (2010) and Pacor, Paolucci, Luzi, *et al.* (2011), records with PGAs and PGVs exceeding a given high percentile of the corresponding distributions are identified as exceptional. Selecting the 95th percentile as the threshold, separately for vertical and horizontal components, 83 such records are recognized within NESS1; 35 of those exceptional records belonging to the 98th percentile of the distribution (Table 2).

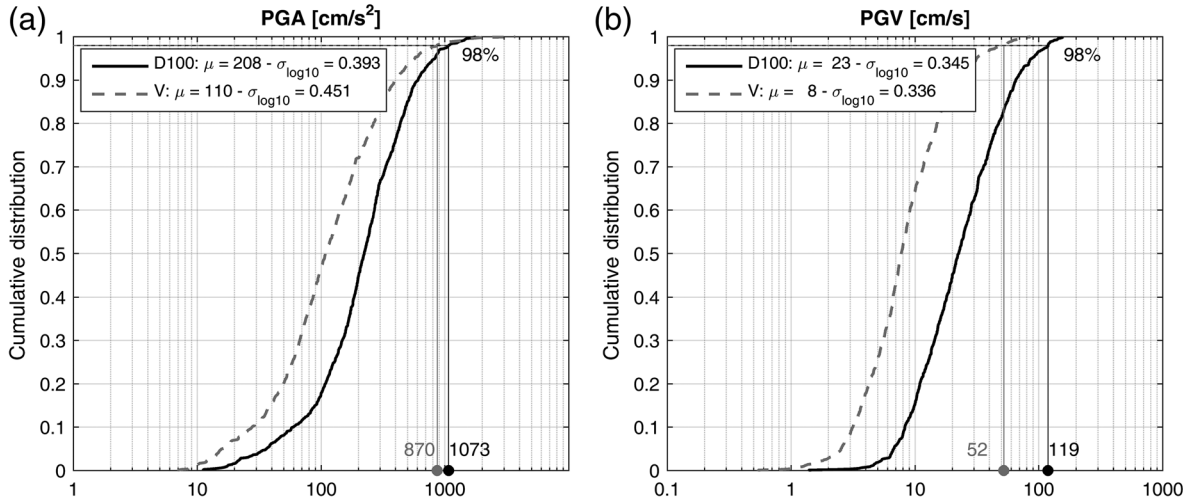

▲ **Figure 3.** Empirical cumulative distribution functions for (a) peak ground acceleration (PGA) and (b) peak ground velocity (PGV) in terms of D100 (solid lines) and vertical component (dashed lines). The reported values 1073 and 870 cm/s^2 for PGA, as well as 119 and 52 cm/s for PGV, indicate the upper second percentiles. Mean and standard deviation (log10 unit) are also reported.

The 83 exceptional records mainly come from Japanese, American, New Zealand, and Italian events. Strike-slip and thrust earthquakes each account for 89% of this subset, whereas the remaining 11% is generated by normal-fault mechanisms. The R_{RUP} of these records varies from 0 to 30 km, and they cover the magnitude range 6.0–8.1 (Fig. 4).

The exceptional PGAs and PGVs do not seem to exhibit a clear dependence on magnitude and distance, similar to those observed in previous empirical studies (Anderson, 2010). They may be related to the complexity of the rupture process, such as the localized failure of different portions of the fault (Hanks and Johnson, 1976; Schmedes and Archuleta, 2008). Moreover, site effects can also play a role in ground-motion amplification: in NESS1, exceptional values are mainly recorded on medium-to-dense deposits, characterized by $V_{S30} < 800$ m/s, and only seven records are recorded on rock site ($V_{S30} \geq 800$ m/s). These ground motions were compared with the predictions of the empirical model, proposed by Campbell and Bozorgnia (2014; hereafter, CB14). Indeed, CB14 was calibrated via more than 7000 data recorded within 80 km from the source, and the authors claim (nonregional) applicability to shallow active-crustal zones. Although CB14 is calibrated for D50 as the IM, the residuals (i.e., the difference between natural logarithms of observations and the CB14 predictions) were computed considering D100 values, to estimate the deviation of the exceptional values with respect to the prediction of the reference model. CB14 is able to describe the NESS1 ground motions, as documented by the PGA and PGV residual distributions that are roughly normally distributed, with almost zero median and standard deviations equal to 0.65 and 0.59, respectively (see Ⓔ Fig. S3).

Figure 5 shows the PGA and PGV epsilons (i.e., the residual divided by the standard deviation of the prediction model) as a function of magnitude, distance, and observed peak parameter. Although no clear trend with magnitude is observed, the majority of the exceptional peak values (black circles) exceeds one standard deviation level, and some data points have an epsilon larger than three. Most of the large epsilon values (> 2) correspond to the highest PGAs and PGVs included in NESS1; this is evident from Figure 5c, in which the number of standard deviations is plotted in function of the observed peak values.

EVIDENCE OF NEAR-SOURCE EFFECTS IN NESS1

In this section, NESS1 is preliminarily analyzed to recognize some well-known near-source features, such as velocity pulse, large vertical ground motion, directionality, and HW effects. Figure 6 shows some NESS1 processed waveforms, as illustrations of characteristic manifestations of these effects. The velocity waveforms at IT.ACC (2016 M_w 6.5 Norcia, Italy, event) and BO.SMN01 (2000 M_w 6.6 Tottori, Japan, earthquake) seem to exhibit typical pulse-like behavior. An example of plausible forward directivity can be observed by comparing the FN velocity traces recorded at the BO.KMM19 and BO.KMM15 stations (2016 M_w 7.0 Kumamoto-shi, Japan, earthquake) that are in opposite positions along the strike direction of the fault: the two velocity waveforms show a different frequency content, with the station that sees most of the rupture propagation happen toward it, that is, KMM15, exhibiting narrow-band, pulse-like characteristics.

Vertical acceleration components exceeding in intensity their horizontal counterparts by a wide margin are observed at stations IT.T1214, and IT.MRN, situated over the faults of the 2016 M_w 6.5 Norcia event and the 2012 M_w 6.0 Emilia second shock (both Italian). Interesting is the vertical acceleration trace at BO.IWT33 station (2008 M_w 6.9 Iwate, Japan, earthquake), located on the HW side of the fault. The waveform is asymmetrical and features an extreme PGA value of almost 4g that is twice the horizontal ones (see Aoi *et al.*, 2008; Suzuki and Iervolino, 2017, for details). On the other hand, the special position of the NZ.WTMC station, close to

Table 2
List of the 35 Exceptional Records (Sorted by Time) within NESS1

Net Code	Station Code	V_{S30} (m/s)	V_{S30} Method	Event ID	Event Name	Event Data Time (yyyy/mm/dd hh:mm:ss)	M_W	FM	R_{RUP} (km)	R_{JB} (km)	D100-PGA (cm/s^2)	D100-PGV (cm/s)	V-PGA (cm/s^2)	V-PGV (cm/s^2)
CE	24207	1031.2	TOPOG	USGS-iscgem787038	San Fernando	1971/02/09 14:00:40	6.7	TF	4.44	3.27	*1436.79*	*119.09*	672.89	*54.25*
A	GZL	327.8	TOPOG	UZ-1976-0001	Gazli	1976/05/17 02:58:41	6.7	TF	5.28	3.67	708.03	63.17	*1186.73*	*61.65*
M	E060	203.2	VS	USGS-usp00013ee	Imperial Valley	1979/10/15 23:16:57	6.5	SS	1	0.1	436.54	*119.11*	*1549.34*	*57.06*
M	5051	348.7	VS	USGS-usp0003afe	Superstition Hills	1987/11/24 13:15:56	6.6	SS	1	0.65	492.78	*155.70*	444.68	32.05
TK	2402	395.0	TOPOG	TK-1992-0002	Erzican	1992/03/13 17:18:39	6.6	SS	1	0.85	478.19	*127.60*	240.83	13.81
M	5453	362.2	TOPOG	USGS-usp00066k9	Northridge	1994/01/17 12:30:54	6.7	TF	13.52	4.64	796.05	*141.96*	468.20	18.55
M	5451	388.4	TOPOG	USGS-usp00066k9	Northridge	1994/01/17 12:30:54	6.7	TF	15.75	0.13	495.44	*119.57*	469.62	23.31
CE	24514	453.9	TOPOG	USGS-usp00066k9	Northridge	1994/01/17 12:30:54	6.7	TF	5.22	1.51	860.37	*132.07*	535.88	19.43
CE	24279	269.0	VS	USGS-usp00066k9	Northridge	1994/01/17 12:30:54	6.7	TF	5.95	3.22	736.06	*120.03*	575.74	33.01
M	5450	389.2	TOPOG	USGS-usp00066k9	Northridge	1994/01/17 12:30:54	6.7	TF	18.97	16.04	674.89	98.83	*872.41*	27.69
CE	24436	257.0	VS	USGS-usp00066k9	Northridge	1994/01/17 12:30:54	6.7	TF	15.75	0.13	*1782.53*	*123.00*	*1059.30*	*74.88*
CE	24207	1031.2	TOPOG	USGS-usp00066k9	Northridge	1994/01/17 12:30:54	6.7	TF	6.82	4.64	*1645.64*	107.36	*1310.93*	50.65
A	496	1374.3	TOPOG	TK-1999-0415	Duzce	1999/11/12 16:57:19	7.3	SS	4.32	0.1	*1073.13*	43.30	317.37	16.71
BO	TTR02	310.0	VS	JP-2000-0007	Tottori	2000/10/06 04:30:17	6.6	SS	1.1	0.98	*1107.49*	*143.47*	775.78	*56.19*
I1	BAM	499.0	VS	IR-2003-0041	Bam	2003/12/26 01:56:53	6.5	SS	1.47	0.1	838.61	*123.27*	*962.55*	39.84
CE	36456	246.0	VS	USGS-nc51147892	Parkfield	2004/09/28 17:15:24	6	SS	2.51	0.24	*1268.79*	89.00	562.52	23.50
BO	NIG15	405.0	VS	JP-2004-0002	Niigata first shock	2004/10/23 08:55:58	6.6	TF	11.35	10.09	*1692.09*	66.50	550.76	13.48
BO	NIG13	372.0	VS	JP-2004-0002	Niigata first shock	2004/10/23 08:55:58	6.6	TF	8.83	0.1	*1502.73*	*132.43*	758.23	28.20
BO	IWT34	371.0	VS	EMSC-20080613_0000091	Iwate	2008/06/13 23:43:46	6.9	TF	5.53	5.49	*1138.79*	57.05	*910.70*	28.10
BO	IWT33	506.0	VS	EMSC-20080613_0000091	Iwate	2008/06/13 23:43:46	6.9	TF	5.09	0.1	*1387.43*	71.30	*3702.31*	*86.19*
NZ	HORC	394.4	TOPOG	EMSC-20100903_0000044	Darfield	2010/09/03 16:35:46	7.1	SS	7.24	7.24	533.04	103.70	653.26	*60.17*
NZ	LINC	358.0	TOPOG	EMSC-20100903_0000044	Darfield	2010/09/03 16:35:46	7.1	SS	7.57	5.38	484.11	116.16	779.84	*76.91*
NZ	GDLC	403.1	TOPOG	EMSC-20100903_0000044	Darfield	2010/09/03 16:35:46	7.1	SS	1.08	1.08	786.94	*151.44*	*1006.78*	39.60
NZ	HPSC	207.0	VS	EMSC-20110221_0000047	Christchurch first shock	2011/02/21 23:51:42	6.2	TF	4.25	4.22	256.10	41.18	*1008.00*	34.86
NZ	D07C	283.0	TOPOG	EMSC-20110221_0000047	Christchurch first shock	2011/02/21 23:51:42	6.2	TF	3.92	3.89	724.17	74.83	*1517.58*	44.49

Data belonging to the 98th percentile of the peak ground motion (peak ground acceleration [PGA] or peak ground velocity [PGV]) distribution for D100 and vertical components are in italics. Network code, station code, V_{S30} values, event-ID, event name, event data time, moment magnitude (M_w), focal mechanism (FM), rupture distance (R_{RUP}), Joyner–Boore distance (R_{JB}) are reported. V_{S30} estimation methods are from VS profile (VS) or topographic proxy (TOPOG).
(Continued next page.)

Table 2 (continued)
List of the 35 Exceptional Records (Sorted by Time) within NESS1

Net Code	Station Code	V_{S30} (m/s)	V_{S30} Method	Event ID	Event Name	Event Data Time (yyyy/mm/dd hh:mm:ss)	M_W	FM	R_{RUP} (km)	R_{JB} (km)	D100-PGA (cm/s^2)	D100-PGV (cm/s)	V-PGA (cm/s^2)	V-PGV (cm/s^2)
NZ	HVSC	352.0	VS	EMSC-20110221_0000047	Christchurch first shock	2011/02/21 23:51:42	6.2	TF	3.35	0.1	*1470.31*	98.96	*1612.63*	41.64
NZ	PRPC	192.0	VS	EMSC-20110221_0000047	Christchurch first shock	2011/02/21 23:51:42	6.2	TF	2.83	2.79	731.35	*122.81*	*1822.04*	49.34
NQ	KATNP	429.3	TOPOG	EMSC-20150425_0000021	Nepal	2015/04/25 06:11:26	7.8	TF	9.61	0.1	160.52	111.18	179.51	*58.29*
BO	KMM16	369.7	TOPOG	USGS-us20005iis	Kumamoto-shi	2016/04/15 16:25:06	7	NF	4.72	0.1	574.58	61.63	387.54	*55.84*
BO	KMM10	280.0	VS	USGS-us20005iis	Kumamoto-shi	2016/04/15 16:25:06	7	NF	1	0.1	*1307.30*	*141.53*	869.51	*52.38*
IT	CLO	420.5	TOPOG	EMSC-20161030_0000029	Norcia	2016/10/30 06:40:18	6.5	NF	1.92	0.1	590.28	69.62	782.02	*68.62*
NZ	KIKS	374.6	TOPOG	EMSC-20161113_0000048	Kaikōura	2016/11/13 11:02:58	8	SS	3.49	0.1	252.46	86.36	242.58	*62.33*
NZ	KEKS	786.3	TOPOG	EMSC-20161113_0000048	Kaikōura	2016/11/13 11:02:58	8	SS	18.78	1.58	*1294.38*	116.03	338.87	*69.01*
NZ	WDFS	378.8	TOPOG	EMSC-20161113_0000048	Kaikōura	2016/11/13 11:02:58	8	SS	20.67	4.8	*1253.87*	107.75	384.39	*54.60*
NZ	WTMC	529.2	TOPOG	EMSC-20161113_0000048	Kaikōura	2016/11/13 11:02:58	8	SS	11.99	0.1	*1103.51*	*119.88*	*1993.14*	46.90

Data belonging to the 98th percentile of the peak ground motion (peak ground acceleration [PGA] or peak ground velocity [PGV]) distribution for D100 and vertical components are in italics. Network code, station code, V_{S30} values, event-ID, event name, event data time, moment magnitude (M_w), focal mechanism (FM), rupture distance (R_{RUP}), Joyner–Boore distance (R_{JB}) are reported. V_{S30} estimation methods are from VS profile (VS) or topographic proxy (TOPOG).

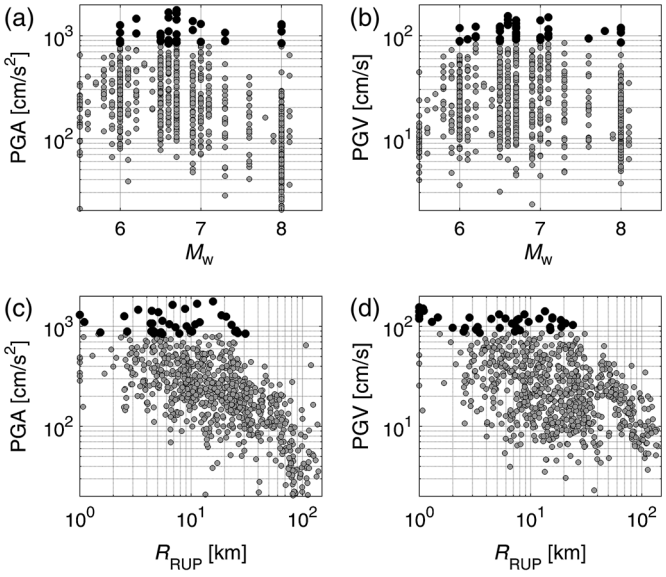

▲ **Figure 4.** (a,b) Magnitude and (c,d) distance scaling of D100 (a, c) PGAs and (b,d) PGVs included in NESS1. The exceptional values are indicated by squares.

the epicenter of the 2016 M_w 8.0 Kaikōura earthquake (New Zealand), resulted in ground motion characterized by horizontal PGA exceeding 1.0g on both horizontal components and a shorter significant duration with respect to those recorded in the near-source region (Bradley *et al.*, 2017).

Some of the strong-motion data included in NESS1 contain the effects of permanent displacement (PD) that is notoriously hard to detect using traditional waveform processing methods. Although such static deformation may be significant for near-source records (e.g., PD > 10 cm), its estimation entails the adoption of baseline correction procedures, the details of which are beyond the scope of this work.

Pulse-Like Ground Motion

In the flat-file compilation, special attention was given to the issue of pulse-like ground motions, due to the engineering relevance of such records. Ground motions with pulse-like characteristics mainly appear when directivity effects combined with the shear-wave radiation pattern lead to constructive wave interference, typically appearing as a double-sided pulse in the velocity signal (Somerville *et al.*, 1997). For the investigation of pulse-like effects within the NESS1 dataset, only records for which instrument orientation was known were considered, that is, 756 out of the 770 in total. The velocity horizontal records were rotated between 0° and 180° and analyzed using the identification algorithm proposed by Baker (2007) to narrow down to a subset of candidate impulsive records and to determine pulse period T_p (Fig. 6a). Based on expert judgement, around 230 records were identified and tagged as pulse-like, most likely due to directivity. The relevant metadata of the pulse identification tag, pulse period T_p, and the indicative pulse orientation are included in the NESS1 flat file, whereas a detailed account of this investigation is presented in a dedicated study (Baltzopoulos *et al.*, unpublished manuscript).

A breakdown of pulse-like records by focal mechanism shows an almost uniform percentage of 30% of total near-source ground motions identified as pulse-like (Fig. 7a). A plot of T_p against M_w is also given (Fig. 7b), showcasing the well-established positive correlation between pulse duration

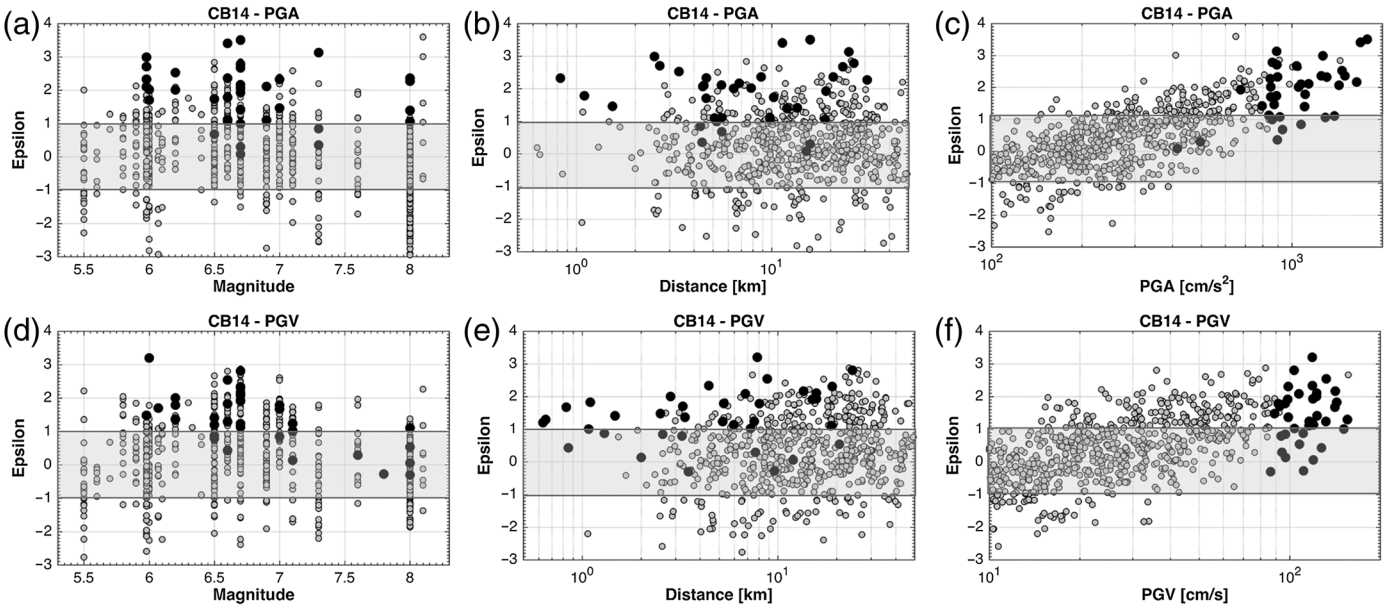

▲ **Figure 5.** Number of standard deviation, epsilon, above and below the CB14 median predictions for (a–c) PGA and (d–f) PGV of NESS1 dataset (gray circles) and the exceptional data (black circles), plotted in (a,d) function magnitude, (b,e) rupture distance, and (c,f) observed peak values. D100 values are used in the plots.

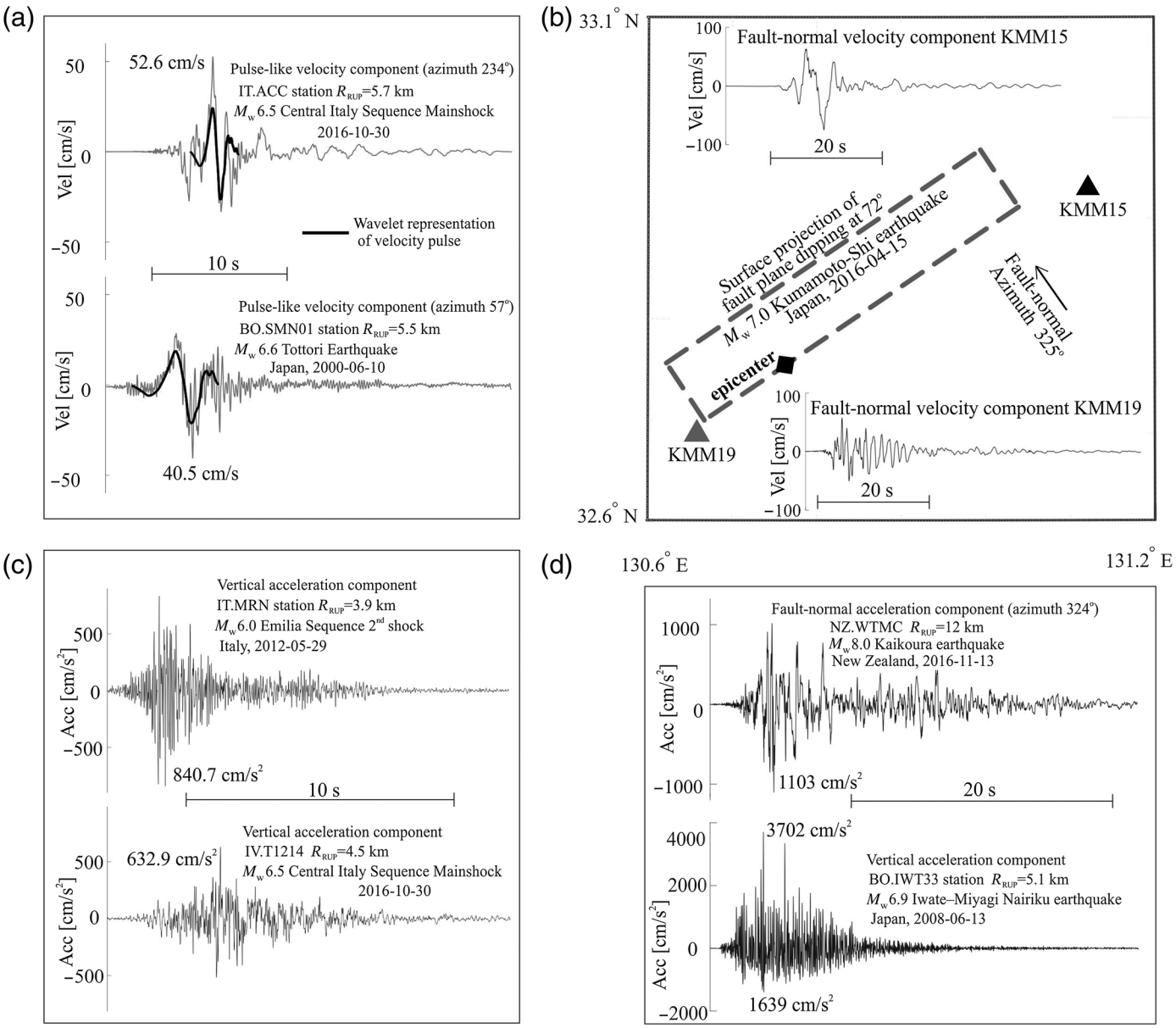

▲ **Figure 6.** Examples of acceleration and velocity waveforms exhibiting evidence of near-source effects. Station code and component orientation are reported together with the moment magnitude M_w and the rupture distance R_{RUP}. PGA and PGV values are also listed. (a) Pulse-like velocity traces recorded at IT.ACC station (2016 M_w 6.5 Norcia, Italy, event) and BO.SMN01 station (2000 M_w 6.6 Tottori, Japan, earthquake) and wavelet representation (Baker, 2007) of the velocity pulse (black thick line); (b) velocity traces (fault-normal components) recorded at two stations, BO.KMM15 and BO.KMM19, that were found in diametrically opposed positions with respect to the fault rupture of the 2016 M_w 7.0 Kumamoto-shi event (Japan); (c) vertical acceleration components recorded at station IT.MRN during the M_w 6.0 second shock of the 2012 Emilia sequence and at IV.T1214 station during the 2016 M_w 6.5 Norcia event; (d) fault-normal horizontal acceleration component recorded at NZ.WTMC station during the 2016 M_w 8.0 Kaikōura earthquake (New Zealand) and vertical acceleration component recorded at BO.IWT33 station during the 2008 M_w 8.0 Iwate earthquake (Japan).

and magnitude (Mavroeidis and Papageorgiou, 2003; Baker, 2007).

Ground-Motion Components

Considerable vertical ground motions, by virtue of being larger than the corresponding horizontal ones, may appear in waveforms recorded at short distances (Bozorgnia and Campbell, 2004; Bindi *et al.*, 2011; Zafarani *et al.*, 2018). V/D50, extracted from NESS1, looks significantly dependent on the natural vibration period T and source-to-site distance (Fig. 8a,b): the largest values occur at short periods, with amplitudes close to 1 or even greater at $T = 0.1$ s for sites over the surface projection of the fault ($R_{JB} < 1$ km). At longer periods, the vertical ground motions are about half of the

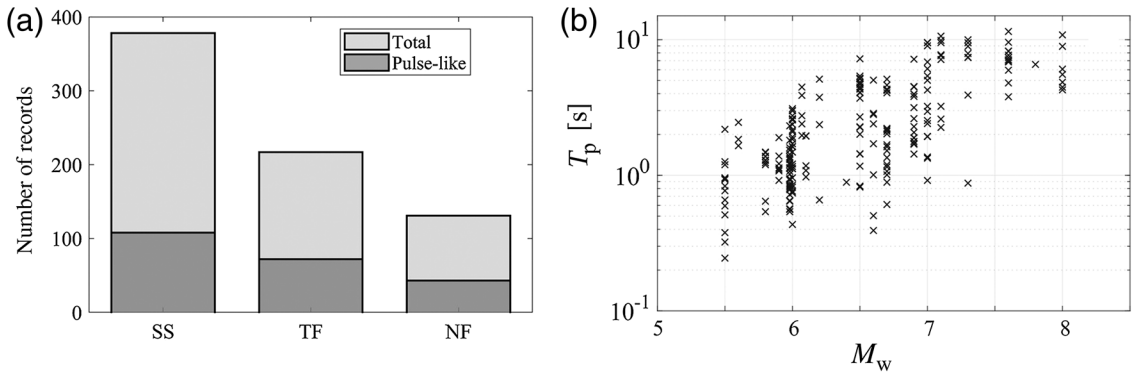

▲ **Figure 7.** (a) Breakdown of pulse-like records identified within the NESS1 dataset by focal mechanism in the histogram format (right): bins of records belonging to strike-slip (SS), thrust-faulting (TF), normal-faulting (NF) events; (b) pulse period versus moment magnitude plot.

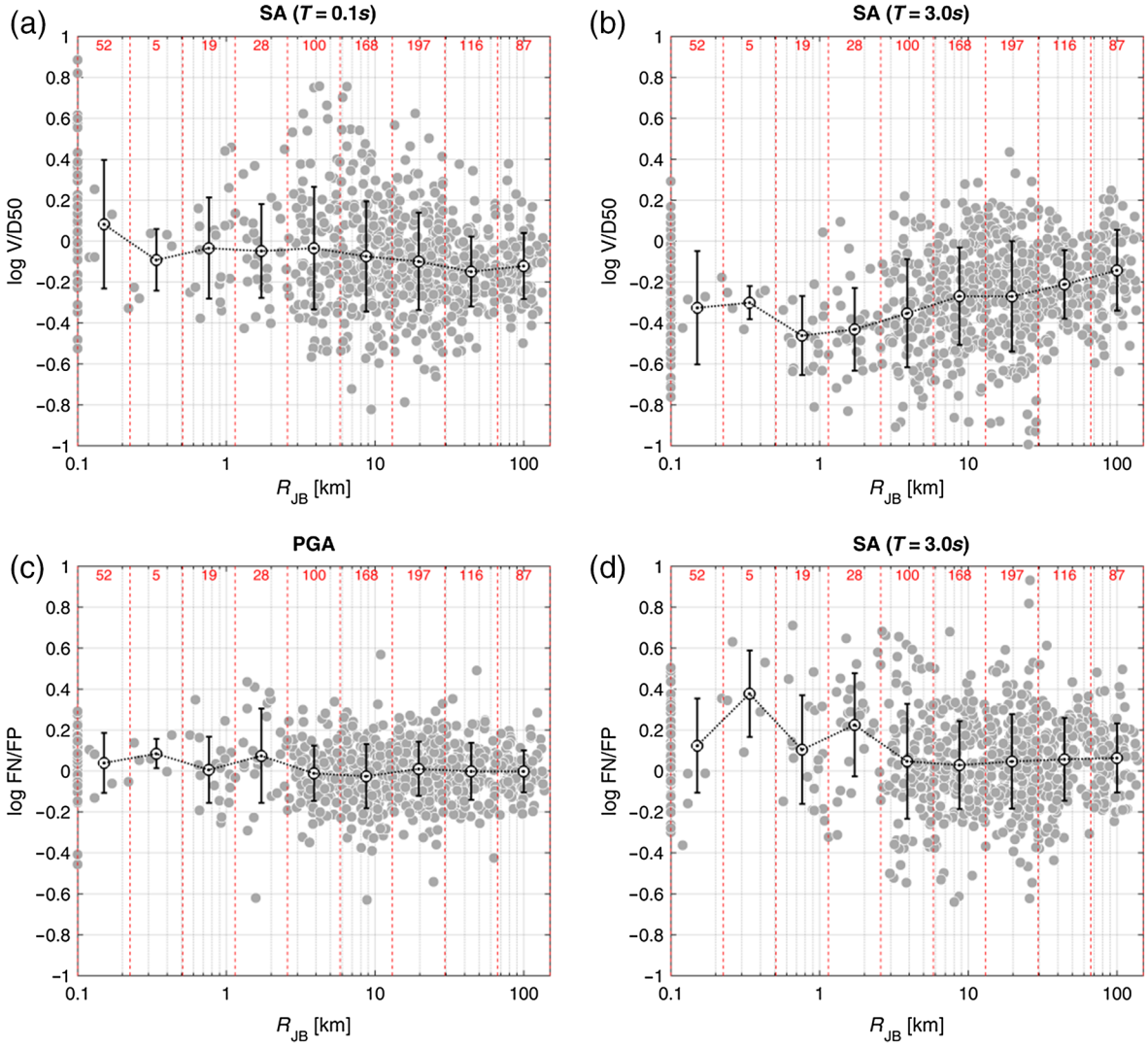

▲ **Figure 8.** Ratios of vertical (V) to D50 for spectral ordinates SA at (a) $T = 0.1$ and (b) $T = 3.0$ s versus Joyner and Boore distance; (c) ratios of fault-normal (FN) to fault-parallel (FP) for PGA and (d) spectral ordinates SA at $T = 3.0$ s. The number of data in each bin is reported. The color version of this figure is available only in the electronic edition.

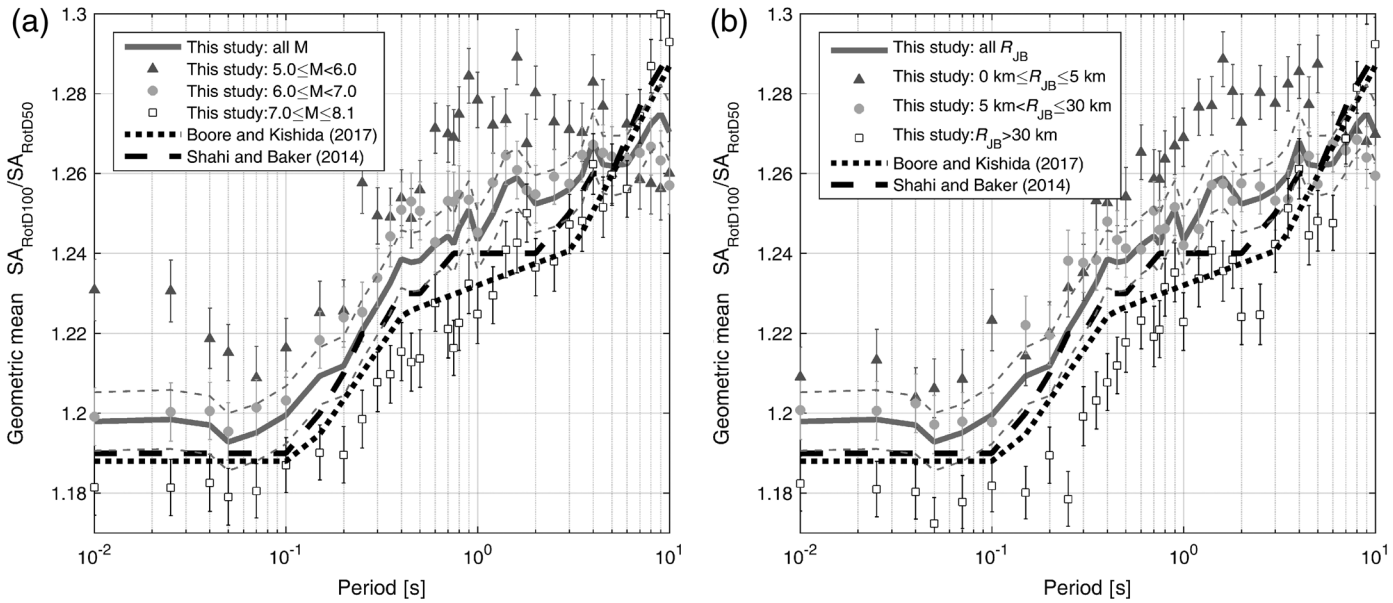

▲ **Figure 9.** (a) D100/D50 ratios for all records and for three magnitude bins, as well as all magnitude bins combined (all magnitudes, the same as $5 \le M_w \le 8$); (b) D100/D50 ratios for all records and for three distance (R_{JB}) bins, as well as all distance bins combined (all distance, the same as $0 \le R_{JB} \le 140$ km). For each period, the D100/D50 is computed as the geometric mean of the ratios for each observation. The bars represent the 95% confidence of the mean. The NESS1 data trend is compared with the models of Boore and Kishida (2017) and Shahi and Baker (2014).

horizontal ones at $R_{JB} < 5$ km and tend to increase at larger distances, possibly also because of surface waves generated during the propagation.

Near-source effects may also determine the polarization of ground motions; as a consequence, the ground-motion intensity in one orientation can be significantly stronger than in others. For this reason, the geometric mean of the as-measured horizontal ground-motion components may hide some features of the shaking in the near-source region. Traditionally, FN and FP orientations are considered important, because some near-source effects (e.g., long-period velocity pulse in FN, fling in FP for strike-slip earthquakes) are generally apparent along these orientations (Sommerville *et al.*, 1997; Mavroeidis and Papageorgiou, 2003). The analysis of the NESS1 dataset shows (Fig. 8c,d) that the FN is larger than FP only at long periods ($T > 1.0$ s) and in proximity of the fault ($R_{JB} < 3$ km). Far from the source, these ratios tend to unity, although the scatter around the mean value is large. These results agree with the findings of Watson-Lamprey and Boore (2007) that showed that the maximum ground motions occurred on the FN direction only at very short distances.

The FN, FP, and vertical (V) ground-motion components have similar values at short vibration periods (see Ⓔ Fig. S4); conversely, at intermediate and long periods, the 50th percentile of the vertical component is about half of the horizontal ones. The difference between FN and FP can be appreciated from intermediate (1.0 s) to long periods (3.0 s), in which the 50th percentile of FN is about 1.5 FP.

Because directional effects appear as an important feature of near-source ground motion, the ratio D100/D50 as a function of period is also investigated, grouping the data in bins of magnitude (Fig. 9a) and distance (Fig. 9b). As observed by Boore (2010), this ratio never exceeds 1.42, corresponding to the value expected for linearly polarized ground motion, and it is almost independent of distance and magnitude. The largest values are observed at long periods close to the fault plane ($R_{JB} < 5$ km). This feature, despite distance bins being poorly sampled up to 5 km, might suggest that source contributions, such as radiation pattern and directivity effects, rapidly vanish with distance. These ratios (averaged over all magnitudes and distances) well agree with the predictions of other studies (Shahi and Baker, 2014; Boore and Kishida, 2017) developed using the NGA-West2 database in the magnitude range 3–8 and distances up to 200 km, and the differences do not exceed 4%, when data at $R_{JB} < 5$ km are considered (see Ⓔ Fig. S4).

Hanging Wall/Footwall

The HW effect is defined as the increase in ground motion at short distances for sites on the HW side of a rupture when compared to sites on the FW side at equal R_{RUP} (Donahue and Abrahamson, 2014), and it is recognizable in case of dip-slip faults. In NESS1, the waveforms relative to reverse and normal events with $|R_X| < 40$ km and $R_{Y0} = 0$ were selected to consider only sites located on the projection of the rupture plane. As shown in Figure 10, the high-frequency ground motions (PGA and SA at $T < 1.0$ s) exhibit systematically higher values on the HW ($R_X > 0$) than those observed on the FW side ($R_X < 0$), whereas no clear dependence on magnitude is observed. On average, the HW amplitude is 2 and 1.5 times the FW amplitude in the distance

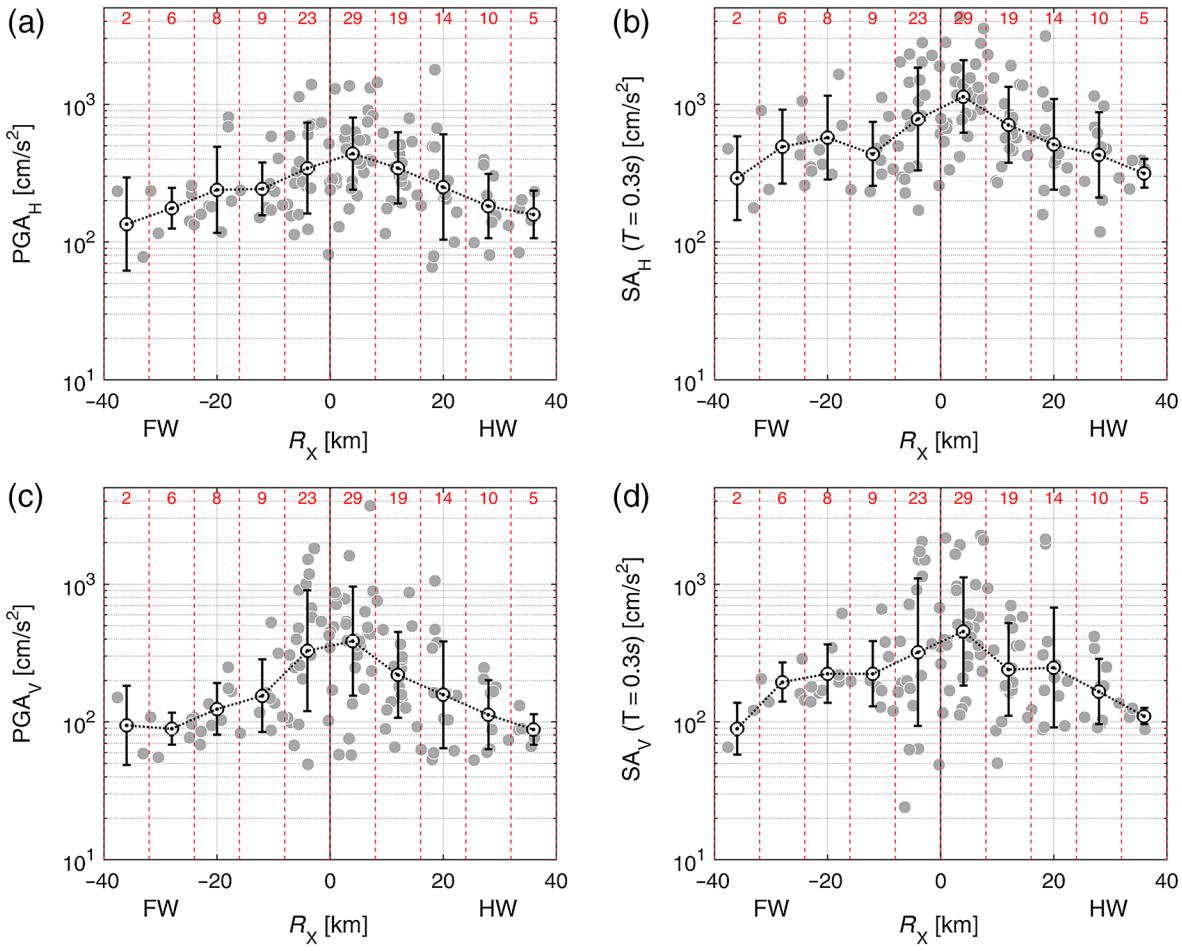

▲ **Figure 10.** PGA and SA at 0.3 s distributions as a function of R_X distance for sites on the hanging wall (HW, $R_X > 0$) and footwall (FW, $R_X < 0$). (a,b) horizontal component; (c,d) vertical component. The number of data in each bin is reported. The color version of this figure is available only in the electronic edition.

range 0–16 km for horizontal (Fig. 10a,b) and vertical (Fig. 10c,d) components, respectively.

FINAL REMARKS

The near strong-motion dataset (named NESS1) is composed of about 800 strong-motion three-component waveforms relative to about 700 accelerometric stations and caused by 74 events with moment magnitudes larger than or equal to 5.5 and hypocentral depths shallower than 40 km, recorded in the time period 1933–2016. The records were selected with the aim of compiling a flat file of ground-motion parameters and associated metadata that can be useful for investigating ground-motion characteristics in the proximity of the seismic source. For this reason, accelerometric data observed within one fault length were included in NESS1.

Event and station metadata were manually reviewed by using the most updated national and international catalogs, studies, and reports. A fundamental step in the compilation of the dataset was to retrieve reliable information about event sources, such as geometries and rupture mechanisms that are key parameters to model relevant near-source effects for engineering applications.

NESS1 only partially overlaps near-source strong-motion data of other published datasets, such as the global NGA-West2 database (Ancheta *et al.*, 2014) and the ESM flat file (Lanzano *et al.*, 2018), mainly including European events for magnitude four and above. About 40% of the NESS1 waveforms are relative to events that occurred in the last five years, thanks to the rapid growth of permanent and temporary networks and the quasi-real-time availability of the raw signals in public web repositories (i.e., the European Integrated Data Archive EIDA, see Data and Resources). More than 20% of the data come from normal-faulting events that are scarcely represented in other global datasets.

A set of preliminary analyses was performed to assess its general representativeness of near-source conditions. First, following previous studies, a subset of records with exceptional peak values was identified. More than 80 records are characterized by a PGA larger than 0.8g or PGVs in excess of 80 cm/s. The majority of these exceptional values are over one standard deviation above the empirical predictions and

some data points are even three times above. These data could improve the evaluation of shaking scenarios in the epicentral area of strong events, if used to better constrain the maximum expected motions and to identify under which physical conditions they occurred.

Evidence of near-source effects was recognized in the NESS1 dataset, such as velocity pulses, large vertical ground motions, directional and HW amplifications, and fling step. These findings substantially confirm existing knowledge from past studies and in particular the following may be worth highlighting.

1. About 30% of the NESS1 data were found to exhibit pulse-like characteristics, that are possibly due to rupture directivity, over a range of orientations. This percentage was almost uniform across focal mechanisms, and the estimated pulse periods' scaling with magnitude was found in agreement with past observations.
2. Differences among the three ground-motion components, in terms of peak and spectral accelerations, are observed in proximity to the source and in narrow frequency bands. At short periods, the ratio between vertical to median horizontal ground-motion intensity is close to 1 or even greater over the rupture fault, whereas it is about 1/2 at long periods; at longer distances, the trend is reversed, it increases at long period and decreases at short period. The largest ground-motion parameters on FN components are only observed at long periods ($T > 1.0$ s) and very close to the fault plane ($R_{JB} < 3$ km), in which the average ratio between FN and FP spectral amplitudes is around 1.5. Finally, the ratio D100/D50 shows a slight dependence on distance, having the largest values close to the source at long periods. The differences with the values predicted by the models of Shahi and Baker (2014) and Boore and Kishida (2017) do not exceed 2%, although the latter are also calibrated including small events and distances up to 200 km.
3. The IMs of waveforms recorded in HW conditions typically exhibit higher values compared to those located in FW at the high frequencies ($T < 1.0$ s). These data may be employed to test the simulation-based models for HW effects.

NESS1 can be a useful tool to investigate the ground shaking in near-source conditions. Further analysis to identify and quantify near-source effects, such as HW amplification, tectonic fling step, and forward directivity can contribute to improving the related predictive models for seismic hazard analysis and, ultimately, performance-based earthquake engineering.

DATA AND RESOURCES

Fault geometries were obtained from: the database of individual seismogenic sources (DISS, http://diss.rm.ingv.it/diss/), the Greek database of seismogenic sources (GreDaSS, http://gredass.unife.it/), the finite-source rupture model database (Mai *et al.*, 2014; SRCMOD, http://equake-rc.info/SRCMOD/, the Next Generation Attenuation relationships for Western U.S. database (Next Generation Attenuation-West2 Project [NGA-West2], https://peer.berkeley.edu/thrust-areas/data-sciences/databases), and the European strong-motion database (ESD, http://www.isesd.hi.is/ESD_Local/frameset.htm).

The locations of the seismic events and the moment magnitudes were obtained from: the International Seismological Centre bulletin (ISC, http://www.isc.ac.uk/iscbulletin/), the Next Generation Attenuation relationships for Western U.S. database, the Istituto Nazionale di Geofisica e Vulcanologia (INGV) bulletin (http://webservices.rm.ingv.it/fdsnws/event/1/), the European–Mediterranean Seismological Centre bulletin (EMSC, http://www.seismicportal.eu/fdsnws/event/1/), the U.S. Geological Survey (USGS, http://earthquake.usgs.gov/), the GeoNet-New Zealand seismic catalog (http://quakesearch.geonet.org.nz/), the Center for Engineering Strong Motion Data (CESMD, http://strongmotioncenter.org/), the ING Catalog (1450 B.C.—1990), the Catalogo della Sismicità Italiana 1981–2002, version 1.1 (CSI, http://cnt.rm.ingv.it/search), the Bollettino Sismico Italiano, Istituto Nazionale di Geofisica e Vulcanologia - Centro Nazionale Terremoti (http://bollettinosismico.rm.ingv.it/), the Global Centroid Moment Tensor Catalog (Global CMT, http://www.globalcmt.org/CMTsearch.html), the U.S. Geological Survey (USGS, http://earthquake.usgs.gov/), the EMSC-CSEM webservice (http://www.emsc-csem.org/Bulletin/), and the European-Mediterranean Regional Centroid Moment Tensors Catalog (RCMT, http://www.bo.ingv.it/RCMT/).

Accelerometric time series were obtained from different online databases: the European Integrated Data Archive (EIDA, https://www.orfeus-eu.org/data/eida/), the GeoNet seismic catalog (https://www.geonet.org.nz/) for New Zealand, the strong-motion seismograph networks of the National Research Institute for Earth Science and Disaster Resilience (http://www.kyoshin.bosai.go.jp/) for Japan, the Unified HEllenic Accelerogram Database (HEAD, http://www.itsak.gr/en/head or http://accelnet.gein.noa.gr) for Greece, the ITalian ACcelerometric Archive (ITACA, http://itaca.mi.ingv.it) for Italy, the National strong-motion Network of Turkey (TR-NSMN, http://kyhdata.deprem.gov.tr/2K/kyhdata_v4.php), the Strong-motion virtual data center (http://strongmotioncenter.org/), the U.S. Geological Survey (https://earthquake.usgs.gov/), the California Geological Survey (http://www.quake.ca.gov/), and the Engineering strong-motion database (ESM, http://esm.mi.ingv.it). The NEar-Source Strong-motion flat-file v0.1 (NESS1) is available at http://ness.mi.ingv.it. All websites were last accessed on September 2018.

ACKNOWLEDGMENTS

This study has been partially developed in the framework of the project RS2: Earthquake simulations and near-source effects, under the Agreement DPC-ReLUIS 2014-2018. The authors are grateful to the Project Coordinator Roberto Paolucci, and to Lucia Luzi, coordinator of the European strong-motion database, for supporting and encouraging the development of this work. The authors are also thankful to

Andrè Herrero for suggesting how to compute the near-source distance. Finally, the authors thank Chiara Maini who contributed to the initial construction of the near-source strong-motion waveforms (NESS) dataset during her thesis work. The authors wish to thank reviewer Annemarie Baltay and one anonymous reviewer for the useful comments and suggestions that improved the quality of our article.

REFERENCES

Aki, K., and P. G. Richards (1980). *Quantitative Seismology*, University Science Books, San Francisco, California.

Allmann, B. P., and P. M. Shearer (2009). Global variations of stress drop for moderate to large earthquakes, *J. Geophys. Res.* **114,** no. B01310, doi: 10.1029/2008JB005821.

Ancheta, T. D., R. B. Darragh, J. P. Stewart, E. Seyhan, W. J. Silva, B. S. J. Chiou, K. E. Wooddell, R. W. Graves, A. R. Kottke, D. M. Boore, *et al.* (2014). NGA-West2 database, *Earthq. Spectra* **30,** no. 3, 989–1005.

Anderson, J. G. (2010). Source and site characteristics of earthquakes that have caused exceptional ground accelerations and velocities, *Bull. Seismol. Soc. Am.* **100,** no. 1, 1–36, doi: 10.1785/0120080375.

Aoi, S., T. Kunugi, and H. Fujiwara (2008). Trampoline effect in extreme ground motion, *Science* **322,** no. 5902, 727–730, doi: 10.1126/science.1163113.

Baker, J. W. (2007). Quantitative classification of near-fault ground motions using wavelet analysis, *Bull. Seismol. Soc. Am.* **97,** no. 5, 1486–1501.

Baltzopoulos, G., C. Eugenio, and I. Iervolino (2015). The displacement coefficient method in near-source conditions, *Earthq. Eng. Struct. Dynam.* **44,** no. 7, 1015–1033.

Bindi, D., F. Pacor, L. Luzi, R. Puglia, M. Massa, G. Ameri, and R. Paolucci (2011). Ground motion prediction equations derived from the Italian strong motion database, *Bull. Seismol. Soc. Am.* **9,** 1899–1920.

Boore, D. M. (2010). Orientation-independent, non geometric-mean measures of seismic intensity from two horizontal components of motion, *Bull. Seismol. Soc. Am.* **100,** 1830–1835.

Boore, D. M., and T. Kishida (2017). Relations between some horizontal-component ground motion intensity measures used in practice, *Bull. Seismol. Soc. Am.* **107,** no. 1, 334–343, doi: 10.1785/0120160250.

Boore, D. M., W. B. Joyner, and T. E. Fumal (1997). Equations for estimating horizontal response spectra and peak acceleration from western North American earthquakes: A summary of recent work (with 2005 erratum), *Seismol. Res. Lett.* **68,** 128–153.

Bozorgnia, Y., and K. W. Campbell (2004). The vertical-to-horizontal spectral ratio and tentative procedures for developing simplified V/H and vertical design spectra, *J. Earthq. Eng.* **4,** no. 4, 539–561.

Bradley, B. A., H. N. T. Razafindrakoto, and V. Polak (2017). Ground-motion observations from the 14 November 2016 M_w 7.8 Kaikoura, New Zealand, earthquake and insights from broadband simulations, *Seismol. Res. Lett.* **88,** no. 3, 740–756, doi: 10.1785/0220160225.

Bray, J. D., and A. Rodriguez-Marek (2004). Characterization of forward-directivity ground motions in the near-fault region, *Soil Dynam. Earthq. Eng.* **24,** no. 11, 815–828.

BSSC (2003). *NEHRP Recommended Provisions for Seismic Regulations for New Buildings and Other Structures* (Fema 450).

Burks, L. S., and J. W. Baker (2016). A predictive model for fling-step in near-fault ground motions based on recordings and simulations, *Soil Dynam. Earthq. Eng.* **80,** 119–126.

Campbell, K. W., and Y. Bozorgnia (2003). Updated near-source ground-motion (attenuation) relations for the horizontal and vertical components of peak ground acceleration and acceleration response spectra, *Bull. Seismol. Soc. Am.* **93,** no. 1, 314–331.

Campbell, K. W., and Y. Bozorgnia (2014). NGA-West2 ground motion model for the average horizontal components of PGA, PGV, and 5% damped linear acceleration response spectra, *Earthq. Spectra* **30,** no. 3, 1087–1115.

Comite Européen de Normalisation (CEN) (2004). *Eurocode 8: Design of Structures for Earthquake Resistance—Part 1: General Rules, Seismic Actions and Rules for Buildings*, CEN European Committee for Standardization, Brussels, Belgium, 229 pp.

Champion, C., and A. Liel (2012). The effect of near-fault directivity on building seismic collapse risk, *Earthq. Eng. Struct. Dynam.* **40,** no. 10, 1391–1409, doi: 10.1002/eqe.1188.

Chioccarelli, E., and I. Iervolino (2010). Near-source seismic demand and pulse-like records: A discussion for L'Aquila earthquake, *Earthq. Eng Struct. Dynam.* **39,** 1039–1062.

Donahue, J. L., and N. A. Abrahamson (2014). Simulation-based hanging wall effects, *Earthq. Spectra* **30,** no. 3, 1269–1284.

Faccioli, E., R. Paolucci, and J. Rey (2004). Displacement spectra for long periods, *Earthq. Spectra* **20,** no. 2, 347–376.

Grimaz, S., and P. Malisan (2014). Near field domain effects and their consideration in the international and Italian seismic codes, *Boll. Geof. Teor. Appl.* **55,** no. 4, 717–738.

Hanks, T. C., and D. A. Johnson (1976). Geophysical assessment of peak accelerations, *Bull. Seismol. Soc. Am.* **66,** no. 3, 959–968.

Hanks, T. C., and H. Kanamori (1979). A moment magnitude scale, *J. Geophys. Res.* **84,** 2348–2350.

Iervolino, I., E. Chioccarelli, and G. Baltzopoulos (2012). Inelastic displacement ratio of near-source pulse-like ground motions, *Earthq. Eng. Struct. Dynam.* **41,** 2351–2357.

Kaklamanos, J., L. G. Baise, and D. M. Boore (2011). Estimating unknown input parameters when implementing the NGA ground-motion prediction equations in engineering practice, *Earthq. Spectra* **27,** no. 4, 1219–1235.

Kamai, R., N. Abrahamson, and R. Gaves (2014). Adding fling effects to processed ground-motion time histories, *Bull. Seismol. Soc. Am.* **104,** no. 4, 1914–1929, doi: 10.1785/0120130272.

Lanzano, G., S. Sgobba, L. Luzi, R. Puglia, F. Pacor, C. Felicetta, M. D'Amico, F. Cotton, and D. Bindi (2018). The pan-European engineering strong motion (ESM) flatfile: Compilation criteria and data statistics, *Bull. Earthq. Eng.*, doi: 10.1007/s10518-018-0480-z.

Lay, T., and T. Wallace (1995). *Modern Global Seismology*, Academic Press, Cambridge, Massachusetts, 521 pp.

Luzi, L., R. Puglia, E. Russo, and ORFEUS WG5 (2016). *Engineering Strong Motion Database, Version 1.0.*, Istituto Nazionale di Geofisica e Vulcanologia, Observatories & Research Facilities for European Seismology, doi: 10.13127/ESM.

Mai, M., and K. K. S. Thingbaijam (2014). SRCMOD: An online database of finite-fault rupture models, *Seismol. Res. Lett.* **85,** no. 6, 1348–1357, doi: 10.1785/0220140077.

Mavroeidis, G. P., and A. S. Papageorgiou (2003). A mathematical representation of near-fault ground motions, *Bull. Seismol. Soc. Am.* **93,** no. 3, 1099–1131.

Pacor, F., R. Paolucci, G. Ameri, M. Massa, and R. Puglia (2011). Italian strong motion records in ITACA: Overview and record processing, *Bull. Earthq. Eng.* **9,** 1741–1759, doi: 10.1007/s10518-011-9295-x.

Pacor, F., R. Paolucci, L. Luzi, F. Sabetta, A. Spinelli, A. Gorini, M. Nicoletti, S. Marcucci, L. Filippi, and M. Dolce (2011). Overview of the Italian strong motion database ITACA 1.0, *Bull. Earthq. Eng.* **9,** no. 6, 1723–1739, doi: 10.1007/s10518-011-9327-6.

Paolucci, R., F. Pacor, R. Puglia, G. Ameri, C. Cauzzi, and M. Massa (2011). Record processing in ITACA, the new Italian strong-motion database, in *Earthquake Data in Engineering Seismology-Predictive Models, Data Management and Networks*, S. Akkar, P. Gülkan, and T. van Eck (Editors), Springer, Dordrecht, The Netherlands, 99–113.

Puglia, R., E. Russo, L. Luzi, M. D'Amico, C. Felicetta, F. Pacor, and G. Lanzano (2018). Strong-motion processing service: A tool to access

and analyse earthquakes strong-motion waveforms, *Bull. Earthq. Eng.* doi: 10.1007/s10518-017-0299-z.

Schmedes, J., and R. J. Archuleta (2008). Near-source ground motion along strike-slip faults: Insights into magnitude saturation of PGV and PGA, *Bull. Seismol. Soc. Am.* **98,** no. 5, 2278–2290.

Shahi, S., and J. W. Baker (2014). NGA-West2 models for ground-motion directionality, *Earthq. Spectra* **30,** 1285–1300.

Somerville, P. G. (2003). Magnitude scaling of the near fault rupture directivity pulse, *Phys. Earth Planet. Int.* **137,** 201–212.

Somerville, P. G., N. F. Smith, R. W. Graves, and N. A. Abrahamson (1997). Modification of empirical strong ground motion attenuation relations to include the amplitude and duration effects of rupture directivity, *Seismol. Res. Lett.* **68,** 199–222.

Spudich, P., B. Rowshandel, S. K. Shahi, J. W. Baker, and B. S. J. Chiou (2014). Comparison of NGA-West2 directivity models, *Earthq. Spectra* **30,** no. 3, 1199–1221.

Suzuki, A., and I. Iervolino (2017). Italian vs worldwide history of largest PGA and PGV, *Ann. Geophys.* **60,** no. 5, S0551, doi: 10.4401/ag-7391.

Thompson, E. M., and A. S. Baltay (2018). The case for mean rupture distance in ground motion estimation, *Bull. Seismol. Soc. Am.* doi: 10.1785/0120170306

Tothong, P., C. A. Cornell, and J. W. Baker (2007). Explicit directivity-pulse inclusion in probabilistic seismic hazard analysis, *Earthq. Spectra* **23,** 867–891.

Wald, D. J., and T. I. Allen (2007). Topographic slope as a proxy for seismic site conditions and amplification, *Bull. Seismol. Soc. Am.* **97,** no. 5, 1379–1395.

Watson-Lamprey, J. A., and D. M. Boore (2007). Beyond SaGMRotI: Conversion to SaArb, SaSN, and SaMaxRot, *Bull. Seismol. Soc. Am.* **97,** 1511–1524.

Wells, D. L., and K. J. Coppersmith (1994). New empirical relationships among magnitude, rupture length, rupture width, rupture area, and surface displacement, *Bull. Seismol. Soc. Am.* **84,** no. 4, 974–1002.

Zafarani, H., L. Luzi, G. Lanzano, and M. R. Soghrat (2018). Empirical equations for the prediction of PGA and pseudo spectral accelerations using Iranian strong-motion data, *J. Seismol.* **22,** no. 1, 263–285, doi: 10.1007/s10950-017-9704-y.

Francesca Pacor
Chiara Felicetta
Giovanni Lanzano
Sara Sgobba
Rodolfo Puglia
Maria D'Amico
Istituto Nazionale di Geofisica e Vulcanologia
via Alfonso Corti, 12
20133 Milan, Italy
francesca.pacor@ingv.it
chiara.felicetta@ingv.it
giovanni.lanzano@ingv.it
sara.sgobba@ingv.it
rodolfo.puglia@ingv.it
maria.damico@ingv.it

Emiliano Russo
Istituto Nazionale di Geofisica e Vulcanologia
Centro Nazionale Terremoti
via di Vigna Murata, 605
00143 Rome, Italy
emiliano.russo@ingv.it

Georgios Baltzopoulos
Iunio Iervolino
Dipartimento di Strutture per l'Ingegneria e l'Architettura
Università degli Studi di Napoli Federico II
via Claudio, 21
80125 Naples, Italy
georgios.baltzopoulos@unina.it
iunio.iervolino@unina.it

Published Online 3 October 2018